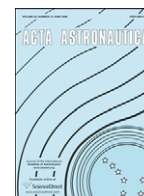




Contents lists available at ScienceDirect

Acta Astronautica

journal homepage: www.elsevier.com/locate/actaastro

A passive, sun-pointing, millimeter-scale solar sail

Justin A. Atchison^{a,*}, Mason A. Peck^b^a Cornell University, Sibley School of Mechanical and Aerospace Engineering, 245 Upson Hall, Ithaca, NY 14853, USA^b Cornell University, Sibley School of Mechanical and Aerospace Engineering, 212 Upson Hall, Ithaca, NY 14853, USA

ARTICLE INFO

Article history:

Received 5 August 2009

Received in revised form

20 November 2009

Accepted 13 December 2009

Available online 18 January 2010

Keywords:

Solar sails

Solar radiation pressure

Spacecraft scaling

Microsystems

ABSTRACT

Taking inspiration from the orbital dynamics of dust, we find that spacecraft length scaling is a means of enabling infinite-impulse orbits that require no feedback control. Our candidate spacecraft is a 25 μm thick, 1 cm square silicon chip equipped with signal transmitting circuitry. This design reduces the total mass to less than 7.5 mg and enables the spacecraft bus itself to serve as a solar sail with characteristic acceleration on the order of 0.1 mm/s^2 . It is passive in that it maneuvers with no closed-loop actuation of orbital or attitude states. The unforced dynamics that result from an insertion orbit and a launch-vehicle separation determine its subsequent state evolution. We have developed a system architecture that uses solar radiation torques to maintain a sun-pointing heading and can be fabricated with standard microfabrication processes. This architecture has potential applications in heliocentric, geocentric, and three-body orbits.

© 2009 Elsevier Ltd. All rights reserved.

1. Introduction

Dust particles in space vary in size from a few molecules to 100 μm and have a mass smaller than a few μg . At these length scales, the dust's orbit is significantly affected by many orbital perturbations that are typically irrelevant in spacecraft trajectories. Length scale influences the relative importance of these effects through a combination of area- or length-dependent force and volume-dependent mass, for a more-or-less fixed material density. These accelerations can compete with gravity to produce trajectories sufficiently different from their Keplerian analogues to serve as new mission opportunities. For example, solar radiation pressure (SRP) ejects dust from the solar system; electromagnetic effects capture and eject dust in planet-centered orbits; and aerodynamic drag captures and lands dust without

the high-temperature ablation that larger meteors typically experience. This research is aimed at harnessing these natural, small-body dynamics in order to enable new propulsion techniques and missions based on them.

In pursuit of this goal, we are working to develop a self-contained spacecraft bus dubbed “sprite”, whose length scale enables it to demonstrate useful propellantless propulsion. Inspired by the 1957 Sputnik mission, we focus on a simple, passive, mission design that achieves Sputnik's rudimentary demonstration of spaceflight capability. For three weeks, the 23 in diameter Sputnik I broadcasted its internal temperature and pressure as it orbited. A half century later, we anticipate duplicating Sputnik's achievement using less than one ten-millionth of its mass. This design rethinks and integrates the traditional subsystems (power, propulsion, communications, etc.) into a single silicon microchip spacecraft capable of unlimited Δv . The sprite bus is a 25 μm thick, 1 cm square, 7.5 mg silicon microchip with integrated solar cells and signal-transmitting circuitry, as illustrated in Fig. 1 and described in Section 5. The spacecraft is passive in that it has no sensor feedback or feedback-based

* Corresponding author. Tel.: +1 607 379 0455; fax: +1 607 255 1222.

E-mail addresses: JAA73@Cornell.edu (J.A. Atchison), MP336@Cornell.edu (M.A. Peck).

Nomenclature			
A	area of solar sail, m^2	W_0	solar energy flux at distance r_0 from the sun, $J m^{-2} s^{-1}$
a_0	acceleration due to solar radiation pressure calculated with effective efficiency η , $m s^{-2}$	z	longitudinal variable in a cylindrical coordinate system, m
a	acceleration, $m s^{-2}$	α	solar sail pitch angle, angle between sun direction and sail normal, rad
C	constant relating solar radiation pressure and central planet effects	β	lightness number
c	speed of light, m/s^2	Δv	change in orbital velocity, $m s^{-1}$
d	thickness of solar sail, m	Δv_e	change in orbital velocity required to achieve a given eccentricity change, $m s^{-1}$
E	orbital energy, $J kg^{-1}$	Δv_s	Δv savings, $m s^{-1}$
e	orbital eccentricity	δ_{cp}	position of solar sail center of pressure measured from the body's center-of-mass, m
\hat{e}_s	direction of solar radiation pressure	δ	angular coordinate about a body's axis of rotation, rad
F	force, N	η	effective solar sail efficiency
I	moment of inertia about a spacecraft axis, $kg m^2$	η_{ab}	solar sail coefficient of absorption
k	stiffness constant associated with linearized restoring torque, $N m rad^{-1}$	η_{dr}	solar sail coefficient of diffuse reflection
l	side length of square solar sail, m	η_{sr}	solar sail coefficient of specular reflection
m	mass of spacecraft, kg	θ	azimuthal coordinate in a circular orbit, rad
\hat{n}	solar sail normal direction	κ	mass density, $kg m^{-3}$
n	mean motion of solar sail, $rad s^{-1}$	μ	gravitational constant, $m^3 s^{-2}$
P	solar radiation pressure, $N m^{-2}$	ρ	radial position variable in a cylindrical coordinate system, m
r	orbital position vector from the system barycenter with magnitude r and direction \hat{r} , m	ω	orbital circular angular velocity, $rad s^{-1}$
r_p	orbital position vector from a planet, m		
r_0	reference orbital radius, m	Subscripts	
s	radius of spherical body, m	G	gravitational
t	time, s	SRP	body acted on by solar radiation pressure
v	orbital velocity, $m s^{-1}$		

actuation. In place of traditional thrusters and attitude-control actuators, it exploits small-body dynamics to accomplish maneuvering.

Several other groups are actively and successfully developing monolithic integrated-circuit (IC) silicon spacecraft (sometimes called a “spacecraft-on-a-chip”), notably the Surrey Space Centre [1,2], the Aerospace Corporation [3–5], and the Jet Propulsion Laboratory [6]. Barnhart, Vladimirova, and Sweeting [1] provide an historical summary of these efforts. The primary incentives for these research programs are persuasive: economies of production, reduced launch mass, and distributed sensing opportunities. However, these objectives generally differ from the primary goal of this

work: capitalizing on length scaling to achieve feasible orbit control. These programs envision spacecraft with masses on the order of grams, which are certainly unusually small by any traditional standard but are still thousands of times larger than our target.

This paper focuses on the efficacy of SRP as a means of propellantless propulsion for a millimeter-scale spacecraft. In this context, the millimeter-scale spacecraft is a solar sail [7]. SRP can greatly influence, if not dominate, the orbital behavior of dust. For example, dust detectors on Pioneers 8 and 9 discovered streams of dust on outbound hyperbolic orbits. These streams originate from comets, which shed the dust throughout their orbit. When released near the sun, some of this dust

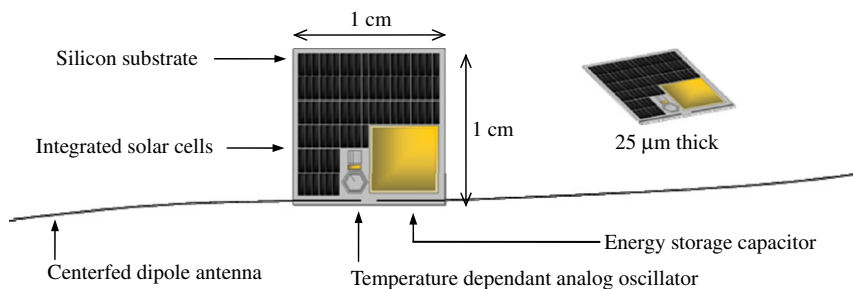


Fig. 1. Sprite bus layout.

experiences a sudden change in acceleration due to solar radiation pressure that sends them on escape trajectories [8–10].

Solar-sail scale has implications not only for performance but also in hardware design and implementation. Typical sail designs are extremely large and combine physical principals that span many orders of magnitude. Greschik [11] suggests that dimensional challenges are primarily responsible for the as yet unsuccessful solar-sail tests, despite 30 years of attempts. The range of magnitudes involved in solar sails make structural analyses intractable, fabrication demanding, and ground testing nearly impossible. These challenges have motivated some to propose and develop so-called solar kites [12], microsolar sails [13], and nanosails that minimize some of these scaling challenges. In August 2008, NASA's NanoSail-D would have been the first spacecraft to demonstrate solar sailing, were it not for the launch-vehicle failure. Like these small solar sail concepts, the millimeter-scale design avoids many of these dimensional issues. It can be fabricated using integrated-circuit techniques and can be readily tested in a 1G environment. However, the millimeter scale offers additional benefits. As this paper argues, it enables more subtle passive behaviors and seeks to capitalize on natural dynamics, avoiding the nontrivial challenges associated with solar-sail control and actuation.

McInnes [8] recognizes the promise of propellantless spacecraft designs that approach centimeter and millimeter scales. He envisions smart, compact sails that use microelectromechanical systems (MEMS) to navigate the solar system autonomously. We pursue that shared vision here by surveying a variety of solar sail maneuvers using passive and feasible attitude control methods and by addressing design and fabrication progress for a candidate spacecraft.

2. Solar radiation pressure

SRP results when sunlight strikes a surface. Photons have energy and momentum related to wavelength. When a photon is absorbed or reflected by a body, momentum is exchanged. This momentum exchange can have a significant, measurable effect on the attitude and orbit of a body illuminated by the sun.

2.1. SRP acceleration

The pressure P from the sun due to this photon momentum transfer is

$$P = \frac{W_0}{c} \left(\frac{r_0}{r} \right)^2 \hat{\mathbf{r}}, \quad (1)$$

where c is the speed of light, W_0 is the energy flux from the sun taken at a distance r_0 from the sun, and $\hat{\mathbf{r}}$ is the direction of the position vector \mathbf{r} with magnitude r . The force \mathbf{F}_{SRP} due to this pressure acting on an opaque sail depends on the surface characteristics, which determine how incoming light is specularly reflected, diffusely reflected, or absorbed. The dimensionless constants η_{sr} , η_{dr} , and η_{ab} account for each of these

respective effects:

$$\mathbf{F}_{SRP} = PA \cos \alpha \left[\left(2\eta_{sr} \cos \alpha + \frac{2}{3}\eta_{dr} \right) \hat{\mathbf{n}} + (\eta_{ab} + \eta_{dr}) \hat{\mathbf{e}}_s \right] \quad (2)$$

$$\eta_{sr} + \eta_{dr} + \eta_{ab} = 1 \quad (3)$$

where A is the area of the sail exposed to photons when facing sunward, α is the sail pitch angle defined by the body's surface-normal unit vector $\hat{\mathbf{n}}$ and the direction $\hat{\mathbf{e}}_s$ of the incoming photons [14]. The acceleration is then

$$\mathbf{a}_{SRP} = \frac{\mathbf{F}_{SRP}}{m}, \quad (4)$$

a term that is proportional to the ratio of the body's area to mass m . A simplified scalar acceleration a_0 is useful when comparing solar sail designs

$$a_0 = 2\eta P \frac{A}{m}. \quad (5)$$

This scalar result is appropriate only for a case in which the sail is facing the sun at a distance of r_0 . Here, the more precise model that is based on the coefficients η_{sr} , η_{dr} , and η_{ab} is replaced by a single efficiency η , henceforth taken to be 0.85 [8]. The ratio of this simplified acceleration to the acceleration due to solar gravity, a_G , is the lightness number β

$$\beta = \frac{a_0}{a_G}. \quad (6)$$

A body's A/m is related to its geometry. In the case of a sphere, a common model for interplanetary dust [15,16], the ratio A/m varies inversely with the body's radius s and mass density κ

$$\frac{A}{m} = \frac{\pi s^2}{\frac{4}{3}\pi \kappa s^3} = \frac{3}{4} \frac{1}{\kappa s}. \quad (7)$$

The acceleration due to SRP is inversely proportional to its characteristic length. This ratio accurately describes the acceleration's dependence on body size for lengths above the wavelength of the sun's spectrum. At length scales below the wavelength of visible light, the particles are simply too small to absorb or scatter the photons. For most materials exposed to sunlight, the critical size is a tenth of a micron [10], a value at which highly reflective particles can achieve $\beta > 1$ and escape solar gravity.

Treating characteristic size as a design parameter, we seek to minimize the size of the sprite spacecraft and replicate the behavior demonstrated by small dust particles. Like most solar sails, the sprite design resembles a flat plate. For such a shape, with its maximum area normal to the sun, A/m simplifies to

$$\frac{A}{m} = \frac{l^2}{\kappa l^2 d} = \frac{1}{\kappa d}, \quad (8)$$

where l is the plate's side length and d is the plate's thickness. Reducing the thickness of the plate or uniformly scaling down all lengths increases the SRP acceleration. This observation motivates the use of ultra-thin 25 μm thick silicon, the thinnest conceivable substrate for an IC. With this thickness, the candidate architecture achieves $a_0=0.10$ mm/s and $\beta=0.0175$. To achieve $\beta > 1$, the thickness would need to be reduced

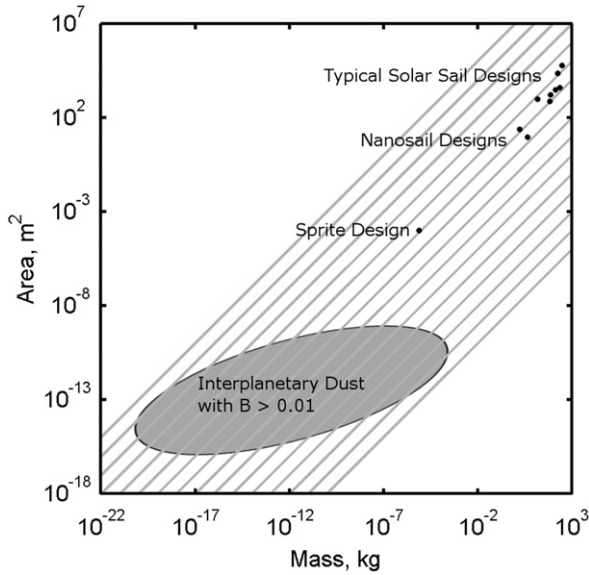


Fig. 2. Sample values of exposed area to mass for dust and solar sails. Diagonal lines show constant A/m contours [8,10,14,17].

to $0.3 \mu\text{m}$. Fig. 2 relates sample values of area and mass for dust and a selection of typical solar sail and nanosail designs. Diagonal lines of constant A/m illustrate that all solar sail designs fall within a comparable A/m ratio. The sprite design is located along these same contours, suggesting that this approach achieves comparable performance to traditional designs.

As bodies absorb solar energy, they experience the so-called Poynting-Robertson drag [17,10]. This drag is associated with a difference in the relativistic Doppler shift between the energy received forwards and backwards with respect to the body’s motion. For dust on bounded heliocentric orbits, this weak drag determines the long-term orbital evolution and eventually collapses these orbits into the sun after thousands of years. The Yarkovsky force is associated with a similar effect: differential thermal radiation of rotating bodies [5]. These effects are weak, even for dust, so we neglect them in this study.

2.2. Coupled attitude and orbital dynamics

SRP accelerations are a function of the orientation of the surface normal vector. Thus the orbital and attitude dynamics of solar sails are coupled in general. The surface of dust is often modeled as homogeneous and spherical for the purposes of calculating β and establishing a normal vector [10]. In this case the normal vector is taken to be constantly sun-pointing. This particular geometry decouples the attitude dynamics from the orbital dynamics [18].

Observations of the mass distribution of dust in the solar system lead some to believe that most dust is spinning very rapidly. Particles that spin rapidly enough may disintegrate via *rotational bursting* [10]. The spin is thought to be generated by “windmill” [19] or “paddle-

wheel” [20] torques that result from SRP acting on dust’s anisotropic surface. These spin rates suggest that the dust particles have non-negligible angular momenta and therefore manifest attitude stiffness. Rather than chaotically tumbling throughout their orbit, the particles may be rapidly spinning with inertially fixed angular momentum vectors. There may be passive dynamical applications for a spinning solar sail, though this paper does not pursue them.

Planning a solar-sail maneuver requires a stable and known heading in the presence of disturbance torques such as free molecular flow, magnetic fields, and gravity-gradient effects. For a plate geometry, however, SRP induced torques likely dominate these effects. An SRP disturbance torque τ is produced if the center of pressure δ_{cp} , where the effective SRP force F acts, does not coincide with the spacecraft’s center of mass [21]

$$\tau = \delta_{cp} \times F_{SRP}. \tag{9}$$

This torque vanishes only when $\delta_{cp} \parallel F_{SRP}$ or $\delta_{cp} = 0$. The first case represents a marginally stable equilibrium heading where the center of pressure is located along the line between the sun and the center of mass. In this orientation, the sail is said to be statically balanced [21,22]. The second case represents an unstable equilibrium that is not practically realizable. An arbitrarily small magnitude of δ_{cp} results in a non-zero torque until the spacecraft reorients and becomes statically balanced. Careful design can minimize the offset, but the required precision is nontrivial. Errors on the order of $100 \mu\text{m}$ can result in a near 90° “edge-on” equilibrium pitch angle. With no access to SRP or solar cell power, this heading is undesirable. Any architecture must therefore account for the likelihood of this disturbance torque.

In the following analysis, we consider an attitude that replicates dust dynamics. We develop methods for achieving a passive sun-pointing attitude. This decouples the attitude and orbital dynamics and offers maximum solar-cell power. The attitude also maximizes the magnitude of SRP by fixing $\alpha=0$. However, the direction of a_{SRP} lies always along the sun line, limiting its use.

3. Applications

This section evaluates orbit opportunities for the given architecture: a passive, sun-pointing solar sail. With these restrictions, the effects of SRP are considered for heliocentric, geocentric, and three-body orbits.

3.1. Two-body heliocentric orbits

The Infrared Astronomical Satellite (IRAS) observed several groupings of dust clearly originating from comets. These groupings follow elliptical heliocentric orbits with non-Keperian parameters which can be explained by SRP [23–25]. In a heliocentric orbit, the sun line is parallel to the orbit-radial direction, $\hat{r} \parallel \hat{e}_s$. In this orientation, SRP effectively reduces the heliocentric gravitational constant μ by the fraction β , which yields a modified two-body

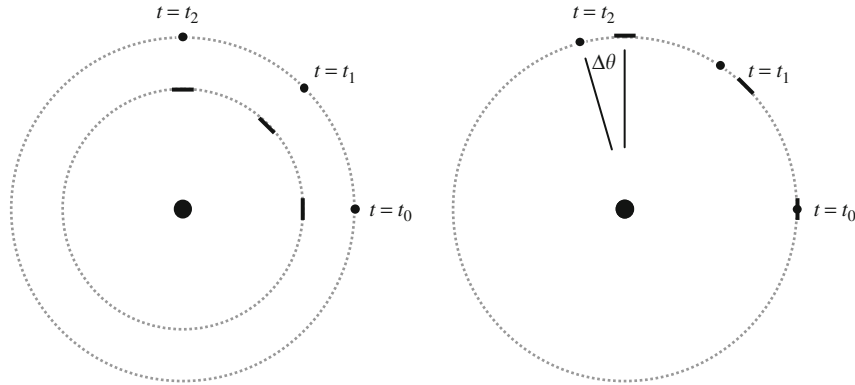


Fig. 3. Simple circular maneuvers enabled by constant sun-pointing attitudes: (a) constant anomaly formation and (b) along-track separation.

equation of motion [26]

$$\ddot{\mathbf{r}} = -\frac{\mu_s(1-\beta)}{r^2}\hat{\mathbf{r}} \quad (10)$$

For $\beta < 1$, this equation produces conic-section orbits with increased orbital energies, as IRAS observed.

As dust particles are released, SRP immediately alters their orbits. While it is still part of the comet, the particle's orbit is negligibly affected by SRP. After release, the particle's new energy E_{SRP} is increased

$$E_{SRP} = \frac{v^2}{2} - \frac{\mu_s(1-\beta)}{r}. \quad (11)$$

If E_{SRP} is positive, the dust escapes on a hyperbolic orbit [9–11]. Streams of these so-called β -meteoroids were detected by both the Galileo [27] and Ulysses [28] missions. In this application, SRP can be thought of as adding an effective Δv to the particle. For a particle released at perihelion, the required β for escape is based on the initial eccentricity e prior to ejection [10]

$$\beta \geq \frac{(1-e)}{2}. \quad (12)$$

One can imagine a similar maneuver for a sun-pointing solar sail. Taking a circular heliocentric orbit at radius r_0 , the minimum impulsive Δv_e required for a spacecraft to achieve a given eccentricity is

$$\Delta v_e = \sqrt{\frac{\mu_s}{r_0}}(\sqrt{1+e}-1). \quad (13)$$

The solar sail escape therefore offers a Δv savings of

$$\Delta v_{savings} = \sqrt{\frac{2\mu}{r_0}}(1-\sqrt{1-\beta}). \quad (14)$$

For the proposed sprite design at 1 AU, Eq. (14) predicts a modest savings of 0.37 km/s, only 3% of the direct escape requirement.

Alternative applications for the modified two-body heliocentric equation of motion have been proposed by the solar-sail community. For example, novel satellite formations can be produced using the modified angular velocity ω of a sun-pointing solar sail in a circular orbit

$$\omega_{SRP} = \sqrt{\frac{\mu_s(1-\beta)}{r^3}}. \quad (15)$$

The radially directed SRP allows two satellites to orbit with the same angular velocity at unique radii [8]. Alternatively, two spacecraft can orbit at the same radius, but with unique angular velocities, perhaps to spread out azimuthally along an orbit. In the first application, a sprite spacecraft at 1 AU could orbit at a radial distance of 880,000 km from a spacecraft that experiences negligible SRP effects, such as a point-mass satellite. In the second application, a sprite spacecraft at 1 AU could be induced to drift at a rate of 31 arcseconds per day (22,500 km per day) along track from a point-mass spacecraft (Fig. 3).

Passive halo or displaced formations are attractive and have been the subject of research [29–31] but require a non-sun-pointing attitude. Here, the sail follows a zero-inclination orbit that is displaced from the ecliptic. McInnes [30] finds that the required pitch angle is a function of the vertical displacement z , the planar radius ρ , the modified angular velocity ω , and the circular Keplerian angular velocity $\omega = \sqrt{\mu/r^3}$

$$\tan \alpha = \frac{\left(\frac{z}{\rho}\right)\left(\frac{\omega_{SRP}}{\omega}\right)^2}{\left(\frac{z}{\rho}\right)^2 + \left[1 - \left(\frac{\omega_{SRP}}{\omega}\right)^2\right]}. \quad (16)$$

This term can be made small but is zero (i.e. sun-pointing) only in the impractical or non-displaced cases of z , ρ , or ω_{SRP} set to zero. The only out-of-plane motion a sun-pointing solar sail experiences must be associated with inclination. This result is intuitive—a reduction in the magnitude of an attractive r^{-2} field does not affect the morphology of the available orbits.

3.2. Two-body geocentric orbits

The effects of SRP on dust in planetary orbits have been well researched, often in conjunction with the rings of Saturn and Jupiter [10,32,33]. SRP is the dominant perturbation at the outer rings, where magnetic fields and tidal forces are weak [34]. Long-term orbit evolution has been evaluated with orbit-averaged perturbation methods that describe the effects of planetary motion about the sun by averaging short term orbit-period effects. After neglecting shadow effects, the orbit-averaged perturbation equations show that semimajor axis is

constant and that the remaining elements vary synchronously with the planet’s period (see for example, Ref. [10], Eqs. (34)–(38)). The change in inclination is proportional to inclination $\Delta i \propto -i$, so equatorial orbits are in a stable equilibrium. These effects were first observed on the Echo I [35] and Vanguard I [36] satellites. Echo I was a communications satellite consisting primarily of a reflective 100 ft diameter mylar balloon [37] ($A/m \approx 0.1 \text{ kg/m}^2$). It demonstrated large-amplitude periodic eccentricity changes, resulting in a perigee altitude that varied annually between 1500 and 930 km [38]. Van der Ha and Modi were the first to consider sun-pointing solar sail maneuvers in a geocentric orbit. They demonstrated secular changes in semimajor axis and semilatus rectum using simple bang-bang control laws [39]. A variety of Earth escape maneuvers have since been analyzed that suppose a solar sail with full attitude control [8].

The prospect of SRP induced periodic change in orbital elements suggests applications for distributed sensing. It is as though a single spacecraft can take measurements from a multitude of traditional orbits. The periodic behavior of inclination for example, enables a spacecraft to sample throughout a range of inclinations annually. For multiple spacecraft, these variations also present a means of gradual propellantless separation.

Hamilton and Krivov [35] offer a special solution for the periodic motion of planetary dust. This solution describes an equatorial, constant-eccentricity orbit whose longitude of pericenter rotates with the planet-sun line (i.e. the periapsis is sun-pointing). This unique orbit is thought to have been identified in Saturn’s “charming ringlet” [40]. The orbit’s eccentricity is related to lightness number

$$e = \frac{C}{\sqrt{1+C^2}}, \tag{17}$$

$$C = \frac{3}{2} \frac{n_{SRP}}{n_p} \frac{a_{SRP}}{a_{GP}}, \tag{18}$$

where n_p and n are the mean motions of the central planet and spacecraft respectively, and a_{GP} is the magnitude of the planet’s two-body gravitational acceleration. Figs. 4 and 5 show the numerical integration of a sample orbit at Earth for $\beta=0.0175$ in both the planet-fixed and sun-planet fixed frames. These figures illustrate two potential applications. In the planet-fixed frame, the spacecraft sweeps through an annulus of space over the course of a year. In this simulation, the apogee of the spacecraft corresponds to geostationary orbit (GEO), so that the spacecraft encounters most or all GEO orbital slots as it is annually precessed. In the sun-planet fixed frame, the orbit stays aligned with Earth’s magnetotail. This orbit may offer scientific sensing applications or applications related to communications satellites.

3.3. Three-body orbits

SRP acting on the orbits of dust in three-body orbits is thought to be observed in the interplanetary dust complex. This is a cloud of dust centered on the ecliptic that causes zodiacal light by bending the sun’s light back

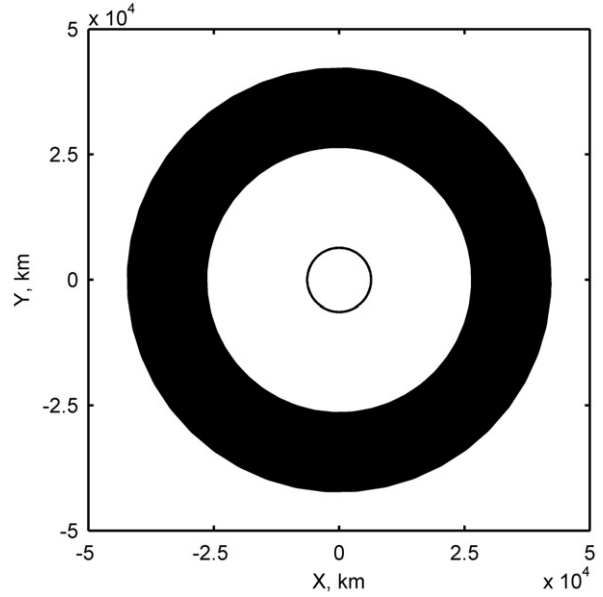


Fig. 4. Earth fixed time history of a geocentric spacecraft with SRP over one-year.

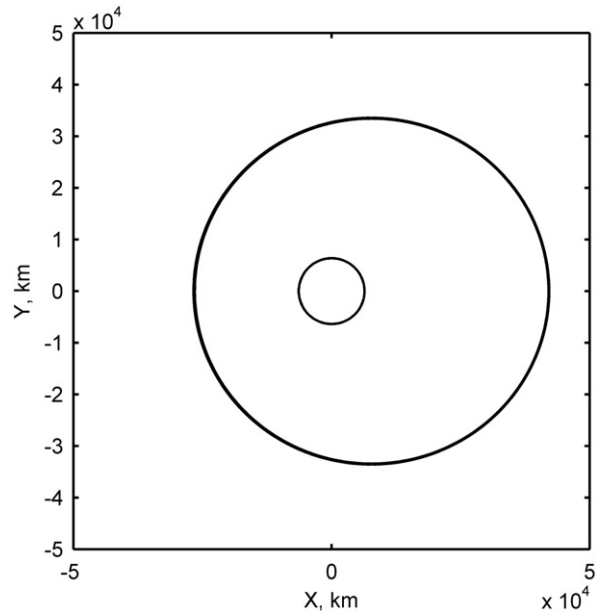


Fig. 5. Sun-Earth fixed time history of a geocentric spacecraft with SRP over one-year. The sun (not shown) is located along the $-X$ axis.

towards Earth [41]. Some of the asymmetries in this cloud are associated with SRP, which groups the dust in regions near modified Lagrange points [42] and in planetary wakes [42,43]. This section evaluates these dynamics and offers potential applications for a spacecraft orbiting in the Sun-Earth system.

The five classical Lagrange points ($L_1 - L_5$) are shifted for a test particle with radially oriented SRP acceleration with $0 < \beta < 1$. The addition of β causes these equilibria to shift along simple paths [43,45,8]. The three collinear

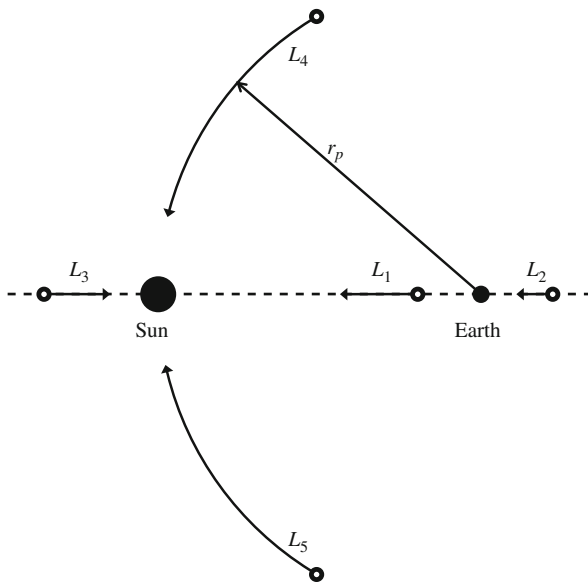


Fig. 6. Motion of the Lagrange points in a corotating reference frame for a sun-pointing spacecraft with increasing β , ($0 \leq \beta \leq 1$) [42].

points move along towards the sun along the Earth–Sun line. The triangular points follow an arc of constant radius r_p towards the sun, as illustrated in Fig. 6.

The Lagrange points are attractive to trajectory designers because they are fixed with respect to the Earth–Sun line. The three collinear points are unstable, so a spacecraft located at those points must expend some energy to maintain its position, albeit a potentially small amount. The triangular points are stable, so bodies (including dust) tend to asymptotically migrate to those locations when nearby. Using a linear analysis, Schuerman [43] shows that the instability of the collinear points is unchanged by the addition of SRP. The triangular points have an added constraint for stability that remains satisfied in the solar system with $\beta < 1$.

In solar sail literature, three-body orbital analyses are common, particularly because many applications are suited to low β sails. A prominent application uses a solar sail with feedback control to both move and stabilize the collinear L_1 point for solar observation [44]. The propellantless nature of solar sails ensures a long lifetime in the presence of disturbance accelerations.

The SRP induced motion of the L_1 point offers applications for solar weather observation. In some cases, the proximity of a spacecraft to the sun is related to the warning time at Earth. For example, coronal mass ejections have characteristic velocities on the order of 500 km/s [45]. As illustrated in Fig. 7, the distance gained at L_1 using SRP can correspond to a significant increase in the warning time at Earth. The lines correspond to maximum, mean, and minimum warning times using 280, 470, and 1000 km/s solar wind speeds [47]. The candidate spacecraft offers approximately 65 min of warning time—an improvement of 13 min over the mass-only case. With enough sprite spacecraft, the sum of these observations could both predict and depict the

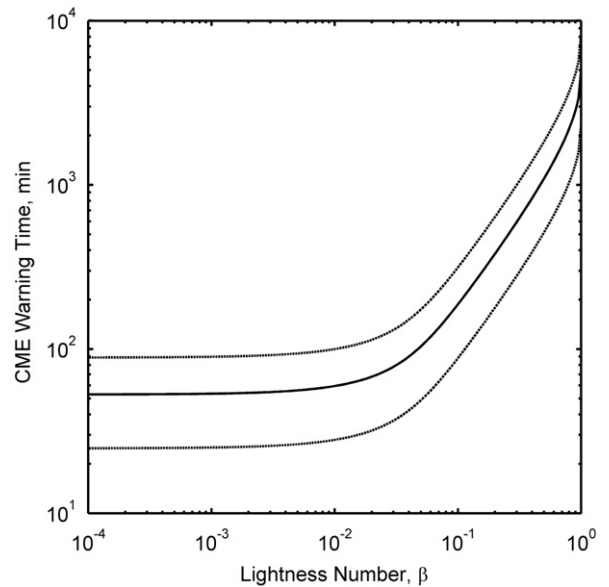


Fig. 7. Estimated CME warning time from L_1 for a spacecraft with increasing β , ($0 \leq \beta \leq 1$).

wave front of earthbound solar phenomena. Though the spacecraft could not stabilize their location, they may experience sufficiently long lifetimes in unstable quasi-periodic orbits to be useful.

4. Passive sun-pointing attitude control

These maneuvers require the design of a suitable attitude architecture that can maintain a sun-pointing heading. As early as 1959, SRP disturbance torques were proposed as a means of attitude actuation [23]. If properly designed, a spacecraft can exploit these torques to produce a stable sun-pointing attitude [46]. Rather than approach this task from a control actuation perspective, we seek geometries that passively align themselves in the presence of SRP. A sphere, for example, decouples the attitude and orbit mechanics in that it experiences only a radial force, regardless of its orientation [19]. Indeed, one of the first solar sail designs was a spherical balloon proposed by Kraft Ehrlicke [19,47]. These designs are simple, but suffer from low β and limited access for solar cells. Rather than a sphere, the first design we consider bears a resemblance to a sun-pointing cone. Using three of the plate-like sprite spacecraft, we propose forming the corner of a cube, as shown in Fig. 8. Kirpichnikov et al. [48] and van de Kolk and Flandro [49] have demonstrated that this geometry creates a global, marginally stable (about two of three axes) sun-pointing attitude whose nonradial force components cancel in both 2D and 3D orientations. SRP torques orient the composite body such that the three plates' common corner reaches an equilibrium angle with respect to the sun line. For uniform, equal-length plates contemplated here, the axis from the center of mass to the common corner points directly at the sun. The off-axis components of the SRP

force and torques cancel each other, yielding a net force that is directed sunward.

One may be tempted to reorient the spacecraft such that it forms a concave corner-cube retroreflector. This geometry reflects light directly back towards the sun, maximizing the solar pressure’s effect for the given area, and cancelling one of the $\cos(\alpha)$ terms in Eq. (2). However, this equilibrium orientation is naturally unstable [50].

The disadvantage of the stable architecture is a less effective A/m ratio:

$$\frac{A}{m} = \frac{\frac{3}{\sqrt{3}} \rho}{3\kappa l^2 d} = \frac{\sqrt{3}}{3} \frac{1}{\kappa d} \tag{19}$$

An architecture that uses three of the candidate sprite spacecraft yields a lightness number of 0.010. This architecture has the added benefits of redundancy and increased antenna transmission coverage. Some differentiation among the chips may also improve functionality.

A similar concept uses the orientation of surface elements or “facets” to stabilize a sun-pointing plate

spacecraft [50–52]. Each facet produces a torque according to its orientation and surface coating. By strategically placing these facets, the net optical properties can be made to vary with pitch angle. Harris and Wehner [51] designed a radially symmetric pattern of such facets using primary reflection and absorption models. This demonstrated that locally stable orientations can be achieved by coating the faces of half of the facets with either reflective or absorptive material. A rectangular example is shown in Fig. 9. The surface is symmetric when viewed from the top and asymmetric when viewed from other angles. When placed in an initially sun-pointing attitude, it will tend maintain that heading in spite of disturbances.

Earlier treatments considered geometries in which primary reflection adequately described the path of impinging light [53,54]. In the geometry under consideration here, secondary reflection cannot be neglected. Even at zero pitch angle, light that is specularly reflected from one facet impinges on the adjacent facet, causing a secondary force. A ray-tracing code captures these effects. The force on each surface or facet is evaluated in terms of that facet’s reflective and absorptive properties, according to Eq. (2). Light that is specularly reflected is propagated to the adjacent facets where this equation is applied a second time. This analysis depends on relatively small pitch angles to avoid the need to represent shadowing effects. In recognition of the likelihood that the surface properties are not ideal, $\eta_{sr}=0.80$ and $\eta_{ab}=0.20$ characterize reflective surfaces, and $\eta_{ab}=1.0$ absorptive surfaces.

The geometry of the spacecraft in this model resembles the spacecraft shown in Fig. 9. The outer millimeter that borders the sail’s surface is etched with 32 and 64 $10\ \mu\text{m}$ deep trenches with 35° and 54° side walls respectively. These angles are dictated by the fabrication method described below. The inner walls are coated to be absorptive, while the outer walls are reflective. Fig. 10 shows the resultant torque about both body aligned axes as the pitch angle is varied. The results indicate that the facets produce a net restoring torque around the sun-pointing equilibrium.

Fig. 11 shows the simulated attitude time history for the spacecraft that begins with a non-equilibrium heading. The numerical results suggest that there is

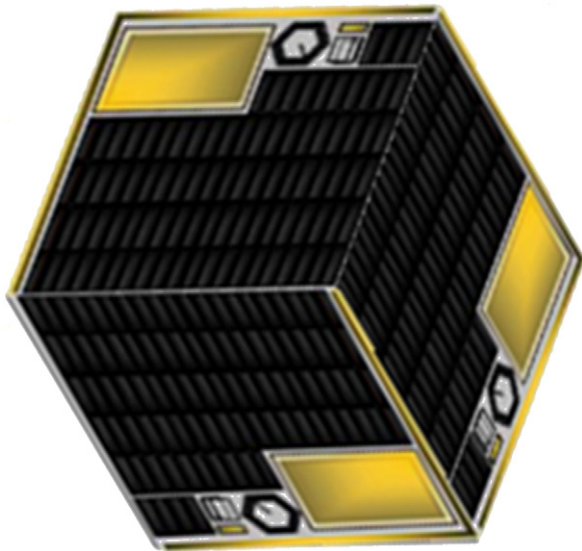


Fig. 8. Stable, sun-pointing corner-cube architecture.

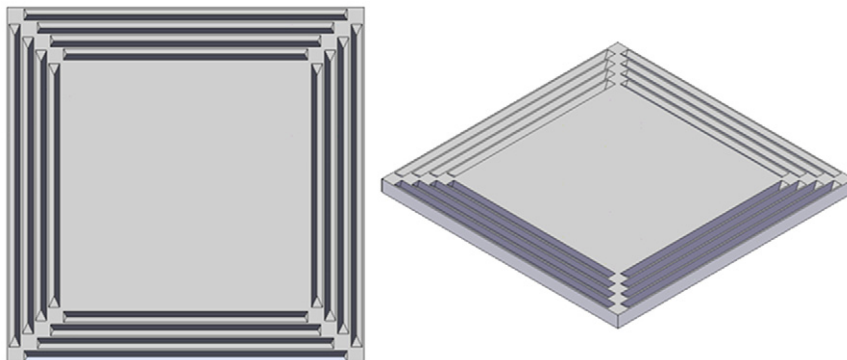


Fig. 9. Faceted surface viewed from top and isometric viewpoints.

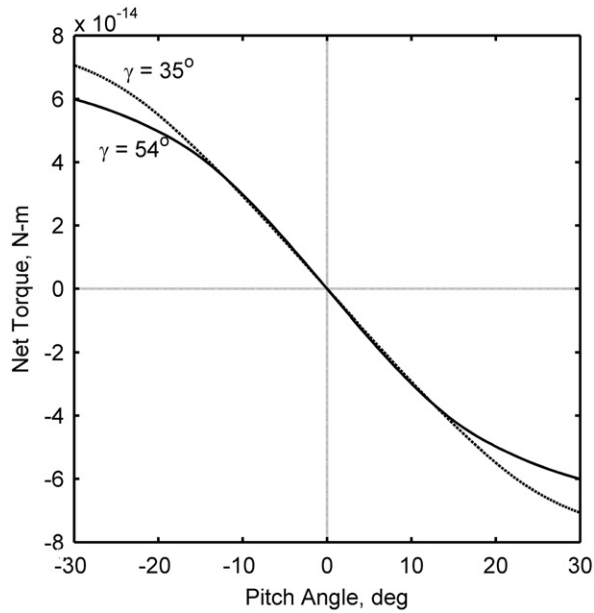


Fig. 10. SRP induced torque as a function of pitch angle for a faceted surface.

negligible loss of net SRP force due to the surface facets. Therefore the effective lightness number remains constant. However, this simulation illustrates two limitations that affect both of these architectures. First, the sun-pointing equilibrium is only marginally stable [23]. Any perturbation tends to produce oscillations about the sun line, as seen in the x and y axes of Fig. 11. These oscillations have a period that can be estimated with a small-angle approximation. The linearized equation of motion about each axis's equilibrium position is

$$I\ddot{\delta} + k\delta = 0, \quad (20)$$

where I is the moment of inertia about the axis and k is a stiffness constant responsible for a linear restoring torque. The familiar natural frequencies for this second order system are the square roots of I/k . For a numerically predicted value of $k = 1.76 \times 10^{-13}$ Nm/rad, we calculate and observe a simulated oscillation period of 120 s. Added structural damping would eliminate these oscillations, perhaps in the form of flexible MEMS beams or thin wire antennas. The second challenge of this architecture is that the attitude motion about the major axis of inertia, here parallel to the sun line, is unregulated. This behavior is evident in the z -axis plot of Fig. 11. Though the magnitude of the pitch angle may be fixed, the orientation of the transverse axes about the sun line is free. A force cannot produce a torque along its direction; so, there is no straightforward architecture that causes SRP to generate a restoring torque about the sun line. Solar gravity gradient cannot be used to constrain this remaining degree of freedom, since it too is radial. Likewise, any active control system requires a sensor input observing a direction other than the sun line. This deficiency prohibits energy-change maneuvers that use a fixed pitch angle, such as simple spiral trajectories [51]. It is possible to use a faceted

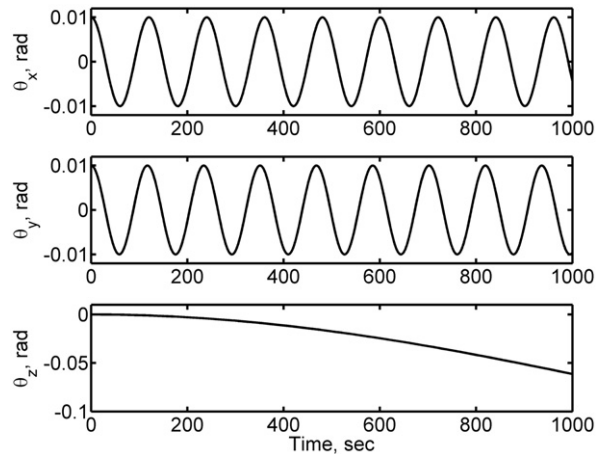


Fig. 11. Attitude time-history for faceted surface with an initial deviation from the sun line.

surface to produce spin-up “windmill” torques about the z -axis. However, with low damping, these torques could ultimately destroy the spacecraft via rotational bursting, as is posited for dust particles.

A surface profile like this one can be fabricated at the microscale with common microfabrication techniques. One straightforward process uses KOH to chemically etch out material along the crystal faces of the silicon substrate. This process produces consistent 54° triangular cuts into the exposed surface of a $\langle 100 \rangle$ aligned silicon plane [53]. This method can produce features in two orthogonal directions along the wafer's surface as dictated by silicon's crystal structure. The fabrication process is outlined in Fig. 12, which shows a profile of the substrate through six steps. Working at the Cornell NanoScale Science & Technology Facility, we demonstrated this process. Fig. 13 shows a Scanning Electron Microscope (SEM) image of our sample wafer with a set of $10 \mu\text{m}$ wide by $7 \mu\text{m}$ deep trenches. This figure shows the end of a trench, where the triangular three-dimensional structure is most visible. Fig. 14 shows the set of trenches after depositing slightly oxidized chrome at a 60° angle from the surface.

5. Candidate microscale infinite-impulse spacecraft bus

Having motivated length scaling of spacecraft, we now explore how small a functional spacecraft can be feasibly produced. Others have asked this same question of spacecraft subsystems and have developed “systems-on-chip,” which integrate traditionally separate components into a single IC package. The result is a low-cost, lightweight, easily-reproducible chip that accomplishes the same tasks as its conventional, large-scale counterpart. Extrapolation suggests that the next step for this technology is to apply the same techniques to an entire spacecraft to create a “spacecraft-on-a-chip.”

We approach this task from a feasibility standpoint, intending to demonstrate functionality at the scales of interest to the dynamic analyses. Thus, we approach the design space with an emphasis on simplicity, achievability,

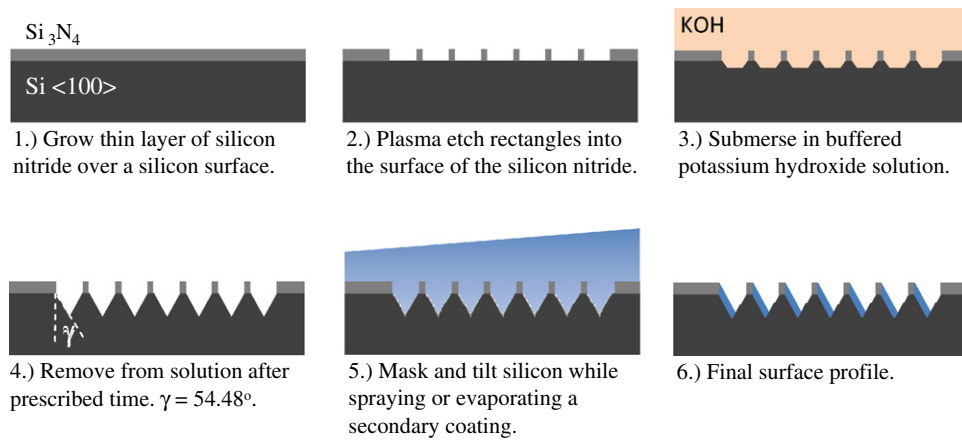


Fig. 12. Anisotropic etching and coating process to produce faceted silicon surface.

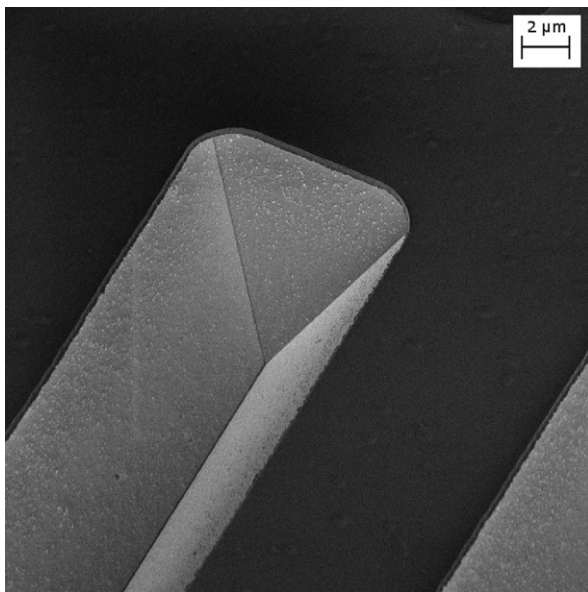


Fig. 13. SEM image of the end of a sample trench in Si coated with Si₃N₄.

and scalability, rather than with an interest in advancing the state of the art in microfabrication. The goal is to design an extremely small demonstration spacecraft bus, in which we can incorporate the SRP propulsion and attitude control architectures described above. In keeping with spacecraft-design convention, we describe this candidate spacecraft bus in terms of eight traditional subsystems.

5.1. Propulsion

Traditional propulsion technologies, such as chemical combustion and ion thrust, cannot be easily scaled to the IC level. An exception is so-called “digital propulsion.” Lewis et al. have successfully fabricated and demonstrated a device that delivers discrete thrust impulses using micron-sized chambers filled with chemical pro-

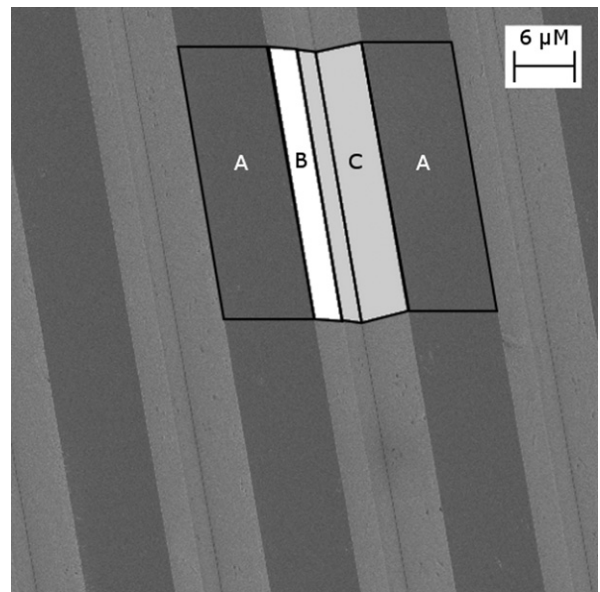


Fig. 14. SEM image of a coated sample trench. (A) Si₃N₄ coated with Cr/Cr₂O₃. (B) Si coated with Cr/Cr₂O₃. (C) Bare Si.

pellant [54]. Though digital propulsion may prove relevant for this research in the long run, the current research is motivated primarily by propellantless propulsion, in hopes of enabling otherwise impossible missions and orbits. SRP, as described above, is among the potential propellantless-propulsion approaches. Future work will include evaluating electromagnetic effects [55] and aerodynamic drag.

5.2. Attitude determination and control

The task of determining and controlling a small spacecraft is perhaps best approached with scaling in mind. Some environmental disturbances may be well suited to producing a known heading. This paper has surveyed methods of achieving locally and globally stable attitude orientations using passive SRP. Torques due to

atmospheric drag, outgassing, and magnetism also may prove useful. Future research will also consider active control, perhaps with MEMS as proposed by McInnes [8].

5.3. Structure

The structure of the spacecraft consists of the volume of semiconductive substrate on which the other subsystems are fabricated. A gallium-arsenide substrate offers improved radiation hardness and the opportunity to produce high-efficiency solar cells. However, the cost of fabricating subsystems on gallium arsenide may discourage its use. We therefore focus on the more common, silicon substrate. At 2300 kg/m^3 , solid silicon is significantly denser than 79 kg/m^3 , the “rule of thumb” density of a typical spacecraft [56]. Nevertheless, the silicon substrate offers the most near-term opportunity to decrease total mass. As a result, we are exploring methods to work with ultra-thin substrates.

Like a traditional structural subsystem, the substrate must support and mechanically interface the other subsystems, facilitate ground handling, and withstand quasistatic loads during transportation and launch. The sprite design is not driven by vibrations due to resonances with either launch or attitude-control inputs because the natural frequencies of such a small structure are far higher than the likely attitude-control bandwidth of any launch vehicle and the sprite itself. Instead, the design is based on the lightest structure on which components can be fabricated: the thinnest possible substrate for a required surface area. For polished silicon wafers, this limit is approximately $200 \mu\text{m}$. Silicon-on-insulator (SOI) wafers are an alternative. Such wafers consist of an ultra-thin layer of silicon on top of a silicon-oxide layer. This substrate offers structural rigidity and handling during fabrication, after which the silicon-oxide layer can be removed to leave the processed device. Then, arbitrarily thin silicon devices can be produced, although the thickness in this paper is restricted to no less than $25 \mu\text{m}$ based on recommendations from experts in silicon fabrication.

We estimate that sufficient functionality can be achieved in 1 cm^2 . The mass of such a 1 cm^2 silicon substrate is 5.75 mg . For conservatism, the mass budget includes 30% margin, yielding a total mass of 7.5 mg , which is used in this paper's calculations. The silicon fabrication process consists of additive and subtractive processes, which add or remove material from the substrate to form a device. The net contribution of these processes is assumed to be negligible.

5.4. Communications

Following Sputnik's example, we conceive the communications subsystem as a transmit-only beacon. The data consists of a single beep at a single frequency—a binary output based on the presence or absence of the carrier. There is no signal *per se* carried on that frequency. For this simple transmission to be tracked from a ground station, it must be powerful enough to

Table 1
Communications link budget.

Parameter	Value	Units
Frequency	433	Mhz
Carrier-to-noise ratio	10	
Altitude	500	km
Free space loss	−139	dB
Atmospheric attenuation	−2.5	dB
Total transmitter attenuation	−2.0	dB
Receiver system noise temperature	250	K
Noise power	−145	dBW
Receiver gain	32	dB
Bandwidth	1	MHz
Margin	2	dB
Required power to transmitter	10	mW

overcome free-space loss, atmospheric attenuation, and other noise sources. The communication link's carrier-to-noise-ratio C/N is therefore a useful measure of goodness. This ratio is influenced by the signal's frequency, the orbit's altitude, the transmitter's losses and power, atmospheric conditions, and antenna efficiency. Table 1 baselines a downlink communications budget at 433 MHz, an amateur satellite band. A single chip can accomplish only so much. A simple way to close the link budget is to select a ground station with very high gain. For example, a 12 m parabolic dish with a standard figure-of-merit of 0.55 offers 32 dB of gain at 433 MHz [57]. Using such a ground station, the link budget estimates that a C/N ratio of 10 requires approximately 10 mW from 500 km. Barnhart [3] notes that it is infeasible to track such a small spacecraft using radar. By contrast, the proposed architecture features a beacon that transmits continuously, and it therefore serves as means for operators to tune the receiver during the first few passes.

The carrier frequency would likely be generated by a crystal oscillator. The frequency stability of crystal oscillators depends on temperature. This dependence can be characterized and used to infer temperature from the beacon's center frequency. The carrier signal would then be impedance matched to a center-fed half-wave dipole antenna. This antenna consists of two very thin 17 cm stiff filaments radiating from the chip. The chief advantage of this antenna is excellent performance in the absence of a ground-plane, a characteristic not available with smaller microstrip or chip antennas. This antenna also offers a large beamwidth, which is favorable since the attitude won't typically be Earth-pointing. Impedance matching can be achieved with microfabricated capacitors and inductors. In an effort to evaluate these practices, we have fabricated candidate capacitors and inductors in the Cornell NanoScale Science & Technology Facility. For a three layer capacitor with silicon-dioxide as a dielectric, we achieved a capacitance density of 10 nF/cm^2 . Fig. 15 shows a photograph of the most recent inductor that we've produced at $20\times$ magnification. This design is based on a three-layer octagonal design by Craninckx and Steyaert [58].

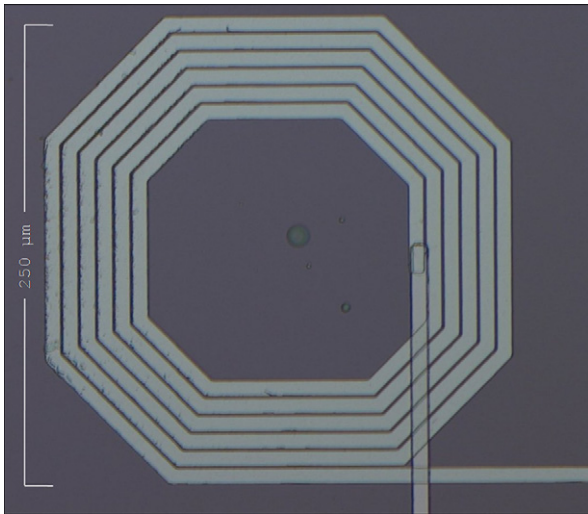


Fig. 15. A 6 loop, 240 μm wide octagonal inductor for the RLC oscillator is shown at $20\times$ magnification.

5.5. Power

Photovoltaic energy harvesting is both passive and based in semiconductor physics, making it a natural choice for power generation in this application. This study baselines silicon-based, first-generation solar cells, which use a single-layer p-n junction diode to pass photovoltaic currents. With strings of individual cells strategically connected in parallel or series, an array can be designed with required voltage and current characteristics to accommodate propulsive, attitude control, or payload requirements. This principle applies equally well to millimeter-scale and macroscopic spacecraft. Commercially available, high-efficiency cells commonly achieve specific power on the order of 200 W/kg. Integrated solar cells are much less efficient [1]. This inefficiency drives the design to devote most of the available silicon surface to photovoltaics. Likewise, electrochemical batteries are difficult to integrate. It may be that a sprite spacecraft simply ought to be powerless in eclipse. Solar cells produce electric power roughly in proportion to the cosine of the pitch angle. For this reason, sun-pointing attitude solutions offer an important advantage over other attitudes.

The power requirements of the communications downlink exceed the available surface area of the chip. Instead, a simple RC-tank charging circuit can produce periodic bursts of power. Solar power charges a capacitor until a critical voltage is reached, at which point a transistor is activated and the stored energy is released to the communications subsystem. By designing the solar cells in series and parallel combinations, we propose a bus voltage of 50 V. This has the advantage of increasing the energy stored in a capacitor, which goes with voltage squared, and can be accommodated with commonly designed high-voltage transistors. This proposed “bursty” operation has a current-limited charging time of roughly 100 ms when fully illuminated by the

Table 2
Power budget.

Parameter	Value	Units
Solar cell		
Efficiency	4.5	mW/cm ²
Area	0.6	cm ²
Voltage	50	V
Current	50	μA
Capacitor		
Charge density	500	nF/cm ²
Area	0.2	cm ²
Capacitance	100	nF
Stored energy	125	μJ
Pulse length	12.5	ms
Available power	10	mW

sun. It then delivers 10 mW to the communications subsystem for 12.5 ms. Table 2 gives relevant power subsystem parameters.

5.6. Payload

In keeping with this simple, feasible, highly integrated design, the one-way communications beacon serves as a means of transmitting spacecraft position and temperature. The orbit may be estimated by incorporating multiple pulses and an orbit-dynamics model into an orbit-determination filter. Position time histories then allow operators to evaluate the effectiveness of the solar sail. The RF carrier frequency indicates the temperature of the crystal oscillator in the communications circuit. We emphasize that this early phase demo may be followed by other applications, with considerably more sophisticated payloads.

We speculate that simple binary signals could be accommodated easily by modulating the carrier frequency with additional capacitance. For example, with a rudimentary Geiger counter, the transmitter could shift the carrier frequency by 0.5 MHz at times when the local impinging radiation exceeded some predefined threshold. Many such signals in a region would depict a time-varying structure within the radiation environment.

5.7. Thermal control

In orbit, this spacecraft's low thermal mass results in temperatures between -130 and 100°C . Temperature changes across this range can occur in tens of seconds [59]. Thermal stresses associated with eclipses may fatigue the chip where dissimilar metals contact. These risks, along with possible mitigation strategies such as microfabricated radiator fins or silicon carbide circuit technologies [60], have yet to be evaluated. An active means of remediation might be achieved by spinning the bus: tilting the attitude so that the face points toward or away from the sun or the earth at an angle that optimizes combined power and thermal performance.

6. Conclusions

This paper presents motivation, analytical evaluation, supporting simulation, and sample designs for a millimeter-scale spacecraft with sufficiently low mass to enable solar sailing. The candidate bus is a $1\text{ cm} \times 1\text{ cm} \times 25\text{ }\mu\text{m}$ silicon IC that conservatively weighs less than 7.5 mg. Each conventional spacecraft subsystem is accounted for and described in the context of a Sputnik-inspired temperature-sensing mission.

Applications to formation and sensing are discussed in the context a sun-pointing spacecraft in heliocentric, Earth, and three-body orbits. If paired with two other millimeter-scale spacecraft to form a corner cube, this design can passively point towards the sun with global attitude stability and use SRP to reduce the effect of solar gravity by 1.0%. This is sufficient to enabling unique formation opportunities. If the design uses microfabricated surface facets instead to produce a locally stable sun-pointing attitude, this acceleration can be improved to 1.75% of sgravity.

Dramatically reducing a spacecraft's mass by replacing the system with a single integrated circuit enables us to capitalize on these perturbations and feasibly accomplish infinite-impulse missions. We are currently working to complete the demonstration chip and begin evaluating its performance in a terrestrial testbed environment.

Acknowledgments

The authors wish to thank Bernardo Cordovez, Zachary Manchester, and Alfred Ernst of Cornell University for extensive design, fabrication, and testing of communications architectures and Dr. Ben Harris for his support and discussion. J. Atchison wishes to thank Dr. Joseph Burns for his introduction to the celestial mechanics of dust.

This work was funded in part by the National Defense Science Engineering Graduate Fellowship and the NASA Institute for Advanced Concepts (Grant 07605-003-071). This work was supported by Sandia National Laboratories through a Center for Integrated Nanotechnologies Grant funded by the Department of Energy. This work was performed in part at the Cornell NanoScale Facility, a member of the National Nanotechnology Infrastructure Network, which is supported by the National Science Foundation (Grant ECS-0335765).

References

- [1] D. Barnhart, T. Vladimirova, M. Sweeting, Very-small-satellite design for distributed space missions, *Journal of Spacecraft and Rockets* 44 (6) (2007) 1294–1306.
- [2] D.J. Barnhart, T. Vladimirova, M. Sweeting, Satellite miniaturization techniques for space sensor networks, *Journal of Spacecraft and Rockets* 46 (2) (2009) 469–472.
- [3] S.W. Janson, Mass-producible silicon spacecraft for 21st century missions, in: AIAA Space Technology Conference & Exposition, Albuquerque, NM, 1999.
- [4] S.W. Janson, H. Helvajian, K. Breuer, MEMS, Microengineering and Aerospace Systems, in: 30th AIAA Fluid Dynamics Conference, AIAA A99-33749, Norfolk, VA, 1999, pp. 1–12.
- [5] S.W. Janson, Micro/nanotechnology for micro/nano/picosatellites, Space 2003, AIAA 2003-6269, Long Beach, CA, 2003, pp. 1–11.
- [6] L.M. Miller, MEMS for space applications, in: Proceedings of Society of Photographic Instrumentation Engineers (SPIE), vol. 3680, Paris, April 1999, pp. 1–13.
- [7] C.R. McInnes, *Solar Sailing: Technology, Dynamics and Mission Applications*, Springer, Berlin, 1999, pp. 1–296.
- [8] M. Harwit, Origins of the zodiacal dust cloud, *Journal of Geophysical Research* 68 (8) (1963) 2171–2180.
- [9] J. Burns, P. Lamy, S. Soter, Radiation forces on small particles in the solar system, *Icarus* 40 (1979) 1–48.
- [10] L. Kresak, Orbital evolution of the dust streams released from comets, *Astronomical Institutes of Czechoslovakia Bulletin* 27 (1) (1976) 35–46.
- [11] G. Greschik, Solar sail scalability and a 'truly scalable' architecture: the space tow, *Journal of Spacecraft and Rockets* 44 (4) (2007) 831–839.
- [12] C. Jack, C.S. Welch, Solar kites: small solar sails with no moving parts, *Acta Astronautica* 40 (2–8) (1997) 137–142.
- [13] V. Lappas, B. Wie, C.R. McInnes, L. Tarabini, L. Gomes, K. Wallace, Microsolar sails for Earth magnetotail monitoring, *Journal of Spacecraft and Rockets* 44 (4) (2007).
- [14] D.A. Vallado, *Solar-Radiation Pressure, Fundamentals of Astrodynamics and Applications*, second ed., Kluwer Academic Publishers, California, 2001, pp. 546–549.
- [15] C. Leinert, E. Grun, *Interplanetary Dust, Physics of the Inner Heliosphere I*, Springer, Berlin, 1990, pp. 207–256.
- [16] P. Staubach, E. Grun, M.J. Matney, Synthesis of Observations, *Interplanetary Dust*, Springer, Berlin, 2001, pp. 347–384.
- [17] H.P. Robertson, Dynamical effects of radiation in the solar system, *Monthly Notices of the Royal Astronomical Society* 97 (6) (1937) 423–438.
- [18] A.A. Shvartsburg, Multishape solar sails: passive achievement of the levitation and slow orbiting stability, in: AIAA Space Programs and Technologies Conference, AIAA-94-4495, Huntsville AL, September 1994, pp. 1–10.
- [19] V.V. Radzievskii, On the influence of an anisotropic re-emission of solar radiation on the orbital motion of asteroids and meteorites, *Astronomicheskii Zhurnal* 29 (1952) 162–170 (In Russian).
- [20] S.J. Paddack, Rotational bursting of small celestial bodies: effects of radiation pressure, *Journal of Geophysical Research* 74 (1969) 4379–4381.
- [21] B. Wie, Solar sail attitude control and dynamics: parts 1 and 2, *Journal of Guidance, Control, and Dynamics* 27 (4) (2004) 526–535.
- [22] R. Sohn, Attitude stabilization by means of solar radiation pressure, *ARS Journal* 29 (5) (1959) 371–373.
- [23] M.V. Sykes, D.M. Hunten, F.J. Low, Preliminary analysis of cometary dust trails, *Advances in Space Research* 6 (7) (1986) 67–78.
- [24] M.V. Sykes, D.J. Lien, The tempel 2 dust trail, *Icarus* 86 (1990) 236–247.
- [25] M.V. Sykes, R.G. Walker, Cometary dust trails, *Icarus* 95 (1992) 180–210.
- [26] H.S. London, Some exact solutions of the equations of motion of a solar sail with a constant setting, *American Rocket Society Journal* 30 (1960) 198–200.
- [27] O. Berg, E. Grun, Evidence of hyperbolic cosmic dust particles, *Space Research XIII* (1973) 1047–1055.
- [28] A. Wehry, I. Mann, Identification of β -meteoroids from measurements of the dust detector onboard the Ulysses spacecraft, *Astronomy and Astrophysics* 341 (1) (1999) 296–303.
- [29] C.R. McInnes, Passive control of displaced solar sail orbits, *Journal of Guidance, Control, and Dynamics* 21 (6) (1998) 975–982.
- [30] S. Gong, J. Li, H. Baoyin, Passive stability design for the solar sail on displaced orbits, *Journal of Spacecraft and Rockets* 44 (5) (2007) 1071–1080.
- [31] S. Gong, J. Li, H. Baoyin, Analysis of displaced solar sail orbits with passive control, *Journal of Guidance, Control, and Dynamics* 31 (3) (2008) 782–785.
- [32] J.W. Chamberlain, Depletion of satellite atoms in a collisionless exosphere by radiation pressure, *Icarus* 39 (1979) 286–294.
- [33] F. Mignard, Radiation pressure and dust particle dynamics, *Icarus* 49 (1982) 347–366.
- [34] D.P. Hamilton, A.V. Krivov, Circumplanetary dust dynamics: effects of solar gravity, radiation pressure, planetary oblateness, and electromagnetism, *Icarus* 123 (0175) (1996) 503–523.
- [35] R.W. Parkinson, H.M. Jones, I.I. Shapire, Effects of solar radiation pressure on earth satellite orbits, *Science* 131 (3404) (1960) 920–921.
- [36] R. Musen, R. Bryant, A. Bailie, Perturbations in perigee height of Vanguard I, *Science* 131 (3404) (1960) 935–936.

- [37] I.I. Shapire, H.M. Jones, Perturbations of the orbit of the echo balloon, *Science* 132 (3438) (1960) 1484–1486.
- [38] R. Bryant, A comparison of theory and observation of the echo I satellite, *Journal of Geophysical Research* 66 (9) (1961) 3066–3069.
- [39] J.C. Van der Ha, V.J. Mode, Orbital perturbations and control by solar radiation forces, *Journal of Spacecraft* 15 (2) (1978) 105–112.
- [40] J. Burt, M.M. Hedman, M.S. Tiscareno, J.A. Burns, The Where and Why of Saturn's Inclined 'Charming Ringlet', *American Astronomical Society, Division of Planetary Sciences Meeting*, vol. 40, p. 445.
- [41] S.F. Dermott, S. Jayaraman, Y.L. Xu, B.A.S. Gustafson, J.C. Liou, A circumsolar ring of asteroidal dust in resonant lock with the Earth, *Nature* 269 (1994) 719–723.
- [42] D.W. Schuerman, The restricted three-body problem including radiation pressure, *The Astrophysical Journal*, Part 1 238 (1980) 337–342.
- [43] W.T. Reach, B.A. Franz, J.L. Weiland, et al., Observational confirmation of a circumsolar dust ring by the COBE satellite, *Nature* 374 (1995) 521–523.
- [44] C.R. McInnes, A.J.C. McDonald, J.F.L. Simmons, E.W. MacDonald, Solar sail parking in restricted three-body systems, *Journal of Guidance, Navigation, and Control* 17 (2) (1994) 399–406.
- [45] J.T. Gosling, Corotating and transient solar wind flows in three dimensions, *Annual Review of Astronomy Astrophysics* 34 (1996) 35–73.
- [46] J. Acord, J.C. Nicklas, Theoretical and practical aspects of solar pressure attitude control for interplanetary spacecraft, *Progress in Astronautics and Aeronautics* 13 (1964) 73–91.
- [47] E. Polyakhova, Space flight using a solar sail—the problems and the prospects, *Kosmicheskiiy Polet Solnechnym Parusom*, Moscow, 1986 (In Russian).
- [48] S. Kirpichnikov, E. Kirpichnikova, E. Polyakhova, Planar heliocentric roto-translatory motion of a spacecraft with a solar sail of complex shape, *Celestial Mechanics and Dynamical Astronomy* 63 (3) (1995) 255–269.
- [49] C.B. van de Kolk, G.A. Flandro, Solar sail passive attitude stability and control, *American Institute of Physics Conference Proceedings* 552 (2001) 373.
- [50] J. Falcovitz, Attitude control of a spinning Sun-orbiting spacecraft by means of a grated solar sail, *Center for Space Research, MIT, CSR TR-66-17*, Cambridge, MA, 1966.
- [51] C.M. Harris, J.W. Wehner, Solar torque control by using thin-film directionally sensitive surfaces, in: *AIAA Guidance, Navigation, and Control Conference*, AIAA 2008-7160, Honolulu, August 2008.
- [52] J.W. Wehner, C.M. Harris, M.K. O'Rell, Solar Torque Control Using Thin Film Directionally Reflective, Emissive, Absorptive, and Transmissive Surfaces, U.S. Patent No. 6,921,050. July 26, 2005.
- [53] K.E. Bean, Anisotropic etching of silicon, *IEEE Transactions on Electron Devices* 25 (10) (1978) 1185–1193.
- [54] D.H. Lewis, S.W. Janson, R.B. Cohen, Digital micropropulsion, *Sensors & Actuators: A Physical* 80 (2) (2000) 143–154.
- [55] J.A. Atchison, M.A. Peck, A millimeter-scale Lorentz propelled spacecraft, in: *Proceedings of the AIAA Guidance, Navigation, and Control Conference*, AIAA-2007-6847, Hilton Head, SC, August 2007.
- [56] E.I. Reeves, *Spacecraft Design and Sizing*, Space Mission Analysis and Design, Kluwer Academic Pub, London, 1999, pp. 301–352.
- [57] F.J. Dietrich, R.S. Davies, Chapter 13: Communications Architecture, *Space Mission Analysis and Design*, Kluwer Academic Pub, London, 1999, pp. 533–586.
- [58] J. Craninckx, M. Steyaert, A 1.8-GHz low-phase-noise CMOS VCO using optimized hollow spiral inductors, *Solid-State Circuits, IEEE Journal of Solid-State Circuits* 32 (5) (1997) 736–744.
- [59] D.G. Gilmore, B.E. Hardt, R.C. Prager, E.W. Grob, W. Ousley, *Spacecraft Subsystems—Thermal*, Space Mission Analysis and Design, Kluwer Academic Pub, London, 1999, pp. 428–458.
- [60] P.G. Neudeck, R.S. Okojie, L.Y. Chen, High-temperature electronics—a role for wide bandgap semiconductors?, *Proceedings of the IEEE* 90 (6) (2002) 1065–1076.